

Depth Super-Resolution from Explicit and Implicit High-Frequency Features

Xin Qiao¹ Chenyang Ge¹ Youmin Zhang² Yanhui Zhou¹
 Fabio Tosi² Matteo Poggi² Stefano Mattoccia²

¹ Xi'an Jiaotong University

² University of Bologna

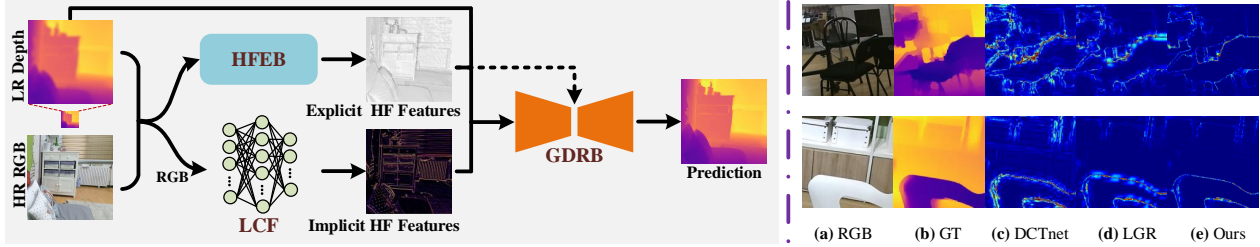


Figure 1. **Depth Super-Resolution exploiting explicit and implicit high-frequency features.** On the left, an overview of our framework, combining the power of both explicit and implicit high-frequency information extracted from the inputs. On the right, qualitative examples with (a) RGB images, (b) ground truth depth and error maps by existing methods (c – d) and ours (e).

Abstract

We propose a novel multi-stage depth super-resolution network, which progressively reconstructs high-resolution depth maps from explicit and implicit high-frequency features. The former are extracted by an efficient transformer processing both local and global contexts, while the latter are obtained by projecting color images into the frequency domain. Both are combined together with depth features by means of a fusion strategy within a multi-stage and multi-scale framework. Experiments on the main benchmarks, such as NYUv2, Middlebury, DIML and RGBDD, show that our approach outperforms existing methods by a large margin ($\sim 20\%$ on NYUv2 and DIML against the contemporary work DADA, with $16\times$ upsampling), establishing a new state-of-the-art in the guided depth super-resolution task.

1. Introduction

With the rise of consumer-grade depth cameras, depth maps are employed in various scenarios such as 3D reconstruction [5, 6], recognition [2] and more. Time-of-Flight (ToF) is one of the leading technologies involved in depth sensing, measuring the distance traveled by emitted rays until they reach points in the scenes. However, due to the limitations of physical fabrication, power consumption and costs [1], the resolution of depth maps usually is often insufficient to fulfill the demand of the downstream applications, such as object detection [9] and pose estimation [18]. In contrast, collecting RGB images at much higher resolution

is cheaper. As a result, the guided depth super-resolution task, known as GDSR, has emerged as a crucial solution to this technological limitation, allowing to obtain an accurate high-resolution (HR) depth map from a low-resolution (LR) one, guided by an HR image.

Initially, algorithms addressing this problem were classified into local [33, 67, 51, 65] and global [13, 47, 16, 38], with the former family being faster, yet suffering in low-textured regions and the latter resulting more robust, at the expense of processing time. More recently, deep neural networks have become the preferred choice for depth super-resolution [26, 36, 37, 42, 60], although they still struggle to restore sharp and precise edges from LR depth maps reliably, especially when dealing with large upsampling factors. This is mainly due to the inadequate guidance provided by High-Frequency (HF) features, implicitly modeled by deep networks, which frequently cause texture copying effects in the upsampled depth maps. In addition, single-stage multi-scale architectures for this task [68, 66, 76, 59], at any given scale, cannot fully leverage fine details encoded at the higher ones, as they are lost due to down-sampling and only partially recovered through skip connections.

In light of the two weaknesses highlighted so far, we aim to improve GDSR by explicitly countering them. For the former, we argue that explicit extraction of HF features, supported by edge detection algorithms such as the Canny operator, can play a crucial role [66]. Concerning the latter, multi-stage network design – which outperforms single-stage counterparts in high-level visual tasks like action segmentation [15] and pose estimation [8], as well as for low-

level vision problems such as image restoration [71, 29] – can mitigate the information loss issue. However, since features extracted from RGB images need to be considered in addition to depth features, existing multi-stage networks are inadequate for GDSR and should be revised to fuse features from the two domains.

In this paper, we present a Depth Super-Resolution method leveraging both Explicit and Implicit HF information (DSR-EI), which contains two branches: the High-Frequency Extraction Branch (HFEB) and the Guided Depth Restoration Branch (GDRB). The former is designed to model **explicit** HF features by exploiting dynamic self-calibrated convolutions (DSP) and the power of vision transformers blocks. The latter effectively fuses the guidance from RGB features with depth features to obtain HR depth maps. This is achieved by deploying two novel modules: 1) the Adaptive Feature Fusion Module (AFFM), which counters the HF information loss due to downsampling, and 2) the Low-Cut Filtering (LCF) module, which acts in the frequency domain to improve **implicit** extraction of HF features. Exhaustive experiments on several standard datasets show the superiority of DSR-EI. In summary, the main contributions of this paper are:

- The proposed architecture employs a novel efficient transformer for explicit, HF feature extraction. The transformer can accurately capture image details and structures from depth maps.
- In the guided depth restoration branch, we propose a low-cut filtering module that can obtain accurate, implicit HF information.
- To counter the information loss issue, we propose an Adaptive Feature Fusion Module located in the middle of the guided depth restoration branch.
- Quantitative and qualitative experimental results demonstrate that our approach establishes a new state-of-the-art in the field of guided depth super-resolution.

Fig. 1 provides a high-level view of our framework, followed by examples that anticipate the superior accuracy achieved by DSR-EI compared to existing methods [74, 11].

2. Related Work

In this section, we first review the literature related to the GDSR task, divided into *conventional* and *learning* methods, as well as to vision transformers.

Conventional Methods. Initially, hand-craft models were developed for GDSR, using the edge co-occurrence between the LR depth map and its HR color counterpart as prior. [33] first utilizes a joint bilateral filter, taking guidance cues from color images. The so-called *local* methods followed this pivotal work: [67] enhances the LR depth maps by exploiting registered HR color images, [51] uses

anti-alias image prefiltering built on the multi-stage joint bilateral filter, while graph-based joint bilateral upsampling [65] casts GDSR as a regularization problem.

More accurate solutions, although slower, are represented by *global* methods. The first work in this direction is [13], which employs Markov random fields (MRF) to integrate multi-modal data for LR depth map upsampling. Using the non-local mean filtering method, [47] recovers noisy LR images from a ToF camera to a high-quality image. To be more efficient, [16] exploits Total Generalized Variation (TGV) regularization for GDSR, enabling a high frame rate. [38] uses fast global smoothing (FGS) to make guided depth interpolation more robust.

Learning Methods. Earlier methods from this category exploit MRF [43, 27, 34]. However, these techniques rely on manually created dictionaries, whose limited content restricts the capacity of generalizing. More recently, deep learning-based approaches achieved remarkable results and became the preferred choice for GDSR. [26] designs a multi-scale guided CNN using hierarchical feature extraction to gradually restores blurred edges. To reconstruct sharp edges, the works by Li et al. [36, 37] learn salient features from color images using an encoder-decoder structure. In contrast, [42] casts GDSR as a pixel-to-pixel mapping from the HR RGB image to the domain of the LR source image, learned by a multi-layer perceptron. In [68], a multi-branch network with progressive refinement performs adaptive information fusion to restore depth details. [66] can quickly upsample depth maps by learning Canny edges, while [76] proposes a depth-guided affine transformation where the feature refinement is carried out iteratively. [59] makes use of implicit neural interpolation, [28] develops a deformable kernel network whose outputs are per-pixel kernels, and [74] proposes a Discrete Cosine Transform Network (DCTNet) to extract multi-modal features effectively. Through graph optimization, [11] combines the advantages of model-driven and deep learning-based methods. Concurrent works exploit recurrent structure attention [69] or combine deep learning with anisotropic diffusion [44].

Despite substantial advancements, these networks are not effective enough at extracting HF guidance from RGB images. Inspired by [41], this paper tackles GDSR leveraging both explicit and implicit HF features guidance.

Vision Transformers. Transformers, initially designed for natural language processing [62], recently gained popularity in computer vision, for tasks such as image recognition [14, 61], object detection [3] and semantic segmentation [64]. Vision Transformers (ViTs) learn long-range dependencies across image tokens through self-attention [20]. Given the natural advantages of such a mechanism, ViTs targeting low-level vision tasks emerged more recently [70, 35, 49], although requiring much larger amounts of parameters and computing resources.

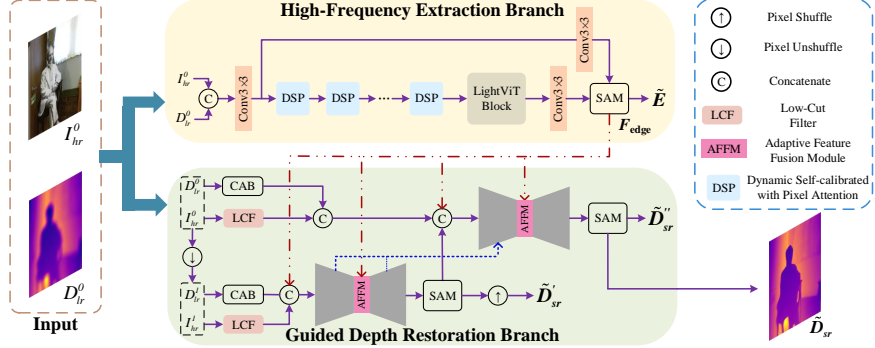


Figure 2: **DSR-EI architecture.** Rectangles with different colors depict different stages and functions in each stage.



Figure 3: **High-frequency information loss (factor 4x).** From left to right, HR depth map and its corresponding gradient map, followed by the gradient map from bicubic upsampled LR depth map and LR depth map itself. HF information is mostly lost in the second gradient map.

3. DSR-EI Framework

In GDSR, HF information in color images – complementary to depth maps – is essential for achieving high performance, which motivates us to seek an efficient method to extract it. In this section, we present our framework that exploits explicit and implicit HF information for depth super-resolution. Then, we introduce the two branches in our network: the High-Frequency Extraction Branch (HFEB) and the Guided Depth Restoration Branch (GDRB).

Fig. 2 shows an overview of our architecture. Given the LR depth map $D_{lr} \in \mathbb{R}^{h \times w \times 1}$ and the corresponding HR color image $I_{hr} \in \mathbb{R}^{H \times W \times 3}$, we aim at restoring HR depth map \tilde{D}_{sr} . Note that $H = s \times h$ and $W = s \times w$, where s denotes the upsampling factor – e.g., $4 \times$, $8 \times$ or even $16 \times$. In our proposed network, the input depth map is firstly upsampled with bicubic interpolation to the same size as I_{hr} . At different scales, we denote the corresponding depth maps and color images as D_{lr}^i and I_{hr}^i , respectively, with $s = 2^i$. Then, according to the above notation, the input images D_{lr}^0 and I_{hr}^0 are fed into the two branches, respectively. Before being sent to GDRB, both the RGB and depth images are processed by a channel-attention block (CAB) [72] and a low-cut filtering (LCF) module, which will be explained in detail in Sec. 3.2.

3.1. High-Frequency Extraction Branch (HFEB)

We argue HF information is crucial for effective super-solving depth and is often lost by upsampling. The primary

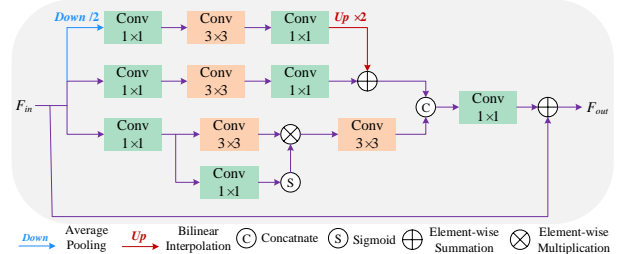


Figure 4: **DSP architecture.** Differently from SCPA [73], our module processes features at different scales, allowing to extract explicit HF information more effectively.

goal of HFEB is to produce an accurate gradient map from an LR depth map, with the support of a color image jointly processed with it.

Indeed, as pointed out in [66], networks for GDSR tend to focus more on depth discontinuities or object boundaries. However, from Fig. 3, we can notice that even with a $4 \times$ factor, most high-frequency information vanishes, as shown by the gradient maps extracted from HR and upsampled LR depth maps, leading to severe degradation of the super-solved depth map. Traditional methods tend to transfer texture to depth maps rather than structural details, failing to extract accurate edges. Moreover, methods extracting binary edges [66] gather insufficient high-frequency information, yielding sub-optimal results.

The work [49] has shown that transformer-based networks can extract clear and meaningful edges by leveraging both global and local features simultaneously. Considering the sparsity of edge maps, we design an efficient transformer, inspired by dynamic scale policy [63] and self-attention [62], to obtain strong HF priors for guiding depth super-resolution. Specifically, our transformer consists of a stack of blocks called dynamic self-calibrated convolution with pixel attention (DSP) and one LightViT block [25]. To better extract HF features, we design the DSP block, which is inspired by SCPA [73] and performs self-calibrated convolution with two branches at a single scale. However, un-

like SCPA, our DSP block includes an additional branch that enables the processing of features at different scales without incurring extra computational burden, as we will demonstrate empirically in our experiments. Specifically, stacked DSP blocks can be expressed as:

$$\Phi_M = \mathcal{F}_{DSP}^M(\mathcal{F}_{DSP}^{M-1}(\dots \mathcal{F}_{DSP}^1(\Phi_0) \dots)) \quad (1)$$

where \mathcal{F}_{DSP}^m denotes the mapping of the m -th DSP block, $m \in [1, M]$, Φ_0 and Φ_M are the input/output features, respectively. As shown in Fig. 4, each DSP block includes three branches: the upper is the dynamic scale branch, the middle is the flat convolution branch, and the lower is the pixel attention branch. Specifically, we employ three convolutions with 1×1 kernel to split the channels, which are further processed by each branch. Note that the dynamic scale branch needs to be downsampled before 1×1 convolution. Except for the pixel attention branch, which has features with half the total channels, the other two branches process features with $\frac{1}{4}$ of the channels each. Next, the pixel attention branch obtains features through the pixel attention scheme [73]. In contrast, the other two branches extract spatial information with a 3×3 flat convolution, followed by a 1×1 convolution to restore the number of channels to be the same as the pixel attention branch. Note that the dynamic scale branch needs upsampling after 1×1 convolution. Then, the features from the dynamic scale and the flat convolution branches can be fused by summation. After concatenation of the features followed by a 1×1 convolution, the DSP finally generates the output features Φ_m in a residual learning fashion.

To further enhance the feature representation of the sub-network, we incorporate LightViT [25] as the tail module, which utilizes local-global attention broadcast to aggregate information from all tokens, allowing for the efficient integration of global dependencies of local tokens into each image token. Finally, considering that the supervised attention module (SAM) [71] can restore information progressively between stages/branches, we employ it to output the gradient map $E \in \mathbb{R}^{H \times W \times 1}$ and high-frequency features $F_{edge} \in \mathbb{R}^{H \times W \times C}$, used respectively as intermediate output – allowing for explicit supervision over edges – and as guidance for GDRB. Under this lightweight design, HFEB can effectively still extract meaningful structural information with different scale receptive fields.

3.2. Guided Depth Restoration Branch (GDRB)

As shown in Fig. 2, GDRB is composed of two stages, and each one processes features at three scales, following a coarse-to-fine strategy [17, 53]. The two stages are implemented with standard U-net architectures [52]. More specifically, a cross-stage feature fusion module [71] is deployed between the two, which proved to be effective in image restoration and, in our design, allows GDRB to benefit

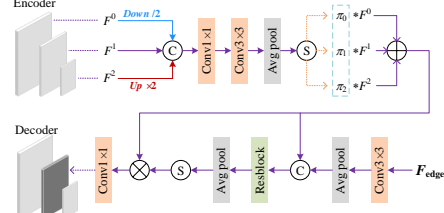


Figure 5: **AFFM architecture, operating at middle scale.** AFFMs for the remaining scales follow the same design.

from the intermediate features extracted by HFEB. To prevent aliasing in downsampling, we employ content-aware filtering layers [75] in the encoders. Besides, GDRB deploys some further SAM blocks [71], allowing valuable features to propagate to the next stage. In addition to depth features, the SAMs of the two stages also output depth maps \tilde{D}'_{sr} and \tilde{D}''_{sr} , to which intermediate supervision is provided. Note that input images are downsampled to the lower stage using pixel unshuffling to prevent information loss. Subsequently, the depth map output of this stage is restored at high resolution by employing pixel shuffling.

Based on the above structure, we propose two novel modules: AFFM and LCF. The former fuses gradient features between each encoder/decoder, while the latter supplements additional HF information in an implicit manner.

Adaptive feature fusion module. Recent networks such as [68, 59] typically concatenate RGB and depth features directly during feature fusion, followed by additional operations such as channel attention [72] to capture useful information. In contrast, inspired by [41], we run adaptive feature fusion through AFFM in two steps to strengthen the reconstruction of HF cues, as illustrated in Fig. 5. We differentiate from [41] by using dynamic convolution [7] to better aggregate depth and HR features. In the first step, we generate dynamic weights $\pi_i, i = 0, 1, 2$, which are then assigned to features from different scales within the current stage. Finally, we perform element-wise summation to obtain the feature maps F' . For clarity, the figure shows the module working at the middle scale of the network as an example, with the others sharing the same design.

In the second step, gradient features F_{edge} from HFEB are concatenated with F' . Then, per-pixel attention maps F_{att} are generated by a ResBlock [22] followed by an average pooling operation. These attention maps are then applied directly to the adaptively fused features F' through element-wise multiplication operation. Finally, after 1×1 convolution, the attention-guided features F_{out}^i are delivered to the corresponding scale of the current stage. In Fig. 5, the output is passed to the middle scale of the decoder. AFFMs working at the other scales send their output to the corresponding scale in the decoder.

Low-cut filtering module. The performance of our

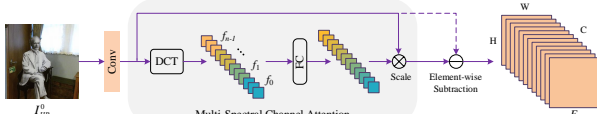


Figure 6: **Low-cut filtering module (LCF).** LF features are extracted through DCT and multi-spectral channel attention, and subtracted from the input to retain HF features.

method greatly benefits from the explicit gradient information, but some valuable high-frequency information still vanishes. This fact motivates us to consider extracting complementary information in the frequency domain. As a common practice [4, 39], we use the low-frequency information of the discrete cosine transform (DCT) to compress images. Based on the design approach proposed in [50], we develop a filtering module utilizing feature decomposition in the frequency domain to extract low-frequency components from the input. Specifically, we apply a 1×1 convolution followed by a channel split to the input color image I^0_{hr} . Then, we can obtain assigned frequency components from the output features $[f_0, f_1, \dots, f_{n-1}]$ after DCT. Thus, the multi-spectral channel attention maps are generated by a fully connected layer and sigmoid activation. According to [50], the low-frequency information is first assured to pass. Thus, we subtract such a low-frequency component from the input features producing the complementary high-frequency features F_{rgb} . Fig. 6 illustrates LCF in detail. The high-frequency cues extracted from these features enable GDRB to progressively super-resolve LR depth maps into HR ones.

Refinement. To enhance the depth quality further, we optionally feed our final output into NLSPN [46] for refinement. This variant of the method is referred to as DSR-EI⁺.

3.3. Training Loss

Our network is trained in an end-to-end fashion using two loss terms: depth loss L_d and gradient loss L_g . The depth loss is defined as:

$$L_d = \|(\tilde{D}_{sr} - D_{gt}) \odot \mathbb{I}\|_1 + \lambda_d \cdot \|(\tilde{D}'_{sr} - D_{gt}) \odot \mathbb{I}\|_1 + \lambda_d \cdot \|(\tilde{D}''_{sr} - D_{gt}) \odot \mathbb{I}\|_1 \quad (2)$$

where D_{gt} is the ground truth depth, \tilde{D}_{sr} , \tilde{D}'_{sr} and \tilde{D}''_{sr} are predicted depth maps from different stages, and \mathbb{I} is pixel validity, as defined in [11]. We empirically set $\lambda_d = 0.2$. Gradient loss L_g is computed on HEFB output, as:

$$L_g = \|\tilde{E} - E_{gt}\|_1 \quad (3)$$

where \tilde{E} is the predicted gradient map and E_{gt} is the ground truth one, extracted according to [41]. Thus, the total loss can be defined as:

$$L_{total} = L_d + \lambda_g \cdot L_g \quad (4)$$

with λ_g empirically set to 0.01.

4. Experimental Results

In this section, we validate the effectiveness of our proposal. We first introduce datasets, metrics and implementation details involved in our evaluation. Then, we compare DSR-EI with state-of-the-art methods, conduct an ablation study on our model and, finally, discuss its limitations.

4.1. Datasets and Metrics

We evaluate DSR-EI on four datasets, compared with existing methods when super-solving depth maps by three different upsampling factors: $4\times$, $8\times$, and $16\times$.

Middlebury[56, 55, 24, 54]. We train all learning-based methods using 50 RGB-D images with ground truth from Middlebury 2005, 2006 and 2014 datasets. As in [11], we retain 5 for validation and 5 for testing.

NYUv2[57]. It contains 1449 RGB-D images in total. Following [11], we randomly split it into 849 RGB-D images for the training set, 300 for the validation set and 300 for the test set. Compared to [68, 40], it comes with a validation set to make the comparison fairer.

DIML[31, 30, 32, 10] consists of 2 million color images and corresponding depth maps from indoor and outdoor scenes. We adopt the same strategy outlined in [11], i.e., considering only the indoor data subset, and use 1440 for training, 169 for validation, and 503 for testing.

RGBDD[23] is a new real-world dataset for GDSR, which consists of 4811 image pairs. For evaluation, we follow the protocol described in [23], using 2215 images (1586 portraits, 380 plants, 249 models) as the training set and 405 images (297 portraits, 68 plants, 40 models) as the test set.

Metrics. Following [11], we compute mean square error (MSE / cm²) and mean absolute error (MAE / cm) as metrics on Middlebury, NYUv2 and DIML. For RGBDD, we use root mean square error (RMSE / cm) as in [23].

4.2. Implementation Details

During training, the HR depth maps and the color images are randomly cropped into 256×256 patches. LR depth patches are generated by bicubic interpolation at 64×64 , 32×32 , 16×16 resolution for $4\times$, $8\times$ and $16\times$ factors, respectively. We randomly extract about 75K, 168K, 223K and 232K patches from Middlebury, NYUv2, DIML and RGBDD for training. Before being fed to the network, depth maps and images are normalized in the $[0, 1]$ range.

We use Pytorch [48] to implement and train DSR-EI, on a single Nvidia RTX 3090 GPU. The batch size is set to 4, using Adam as the optimizer. The learning rate is initialized to 1×10^{-4} , then performing a 5-epoch warm-up and cosine annealing. We use random rotation, horizontal/vertical flipping as data augmentation. According to the size of the four datasets, we train our network for 1505, 198, 155 and 109 epochs on Middlebury, NYUv2, DIML and RGBDD,

Dataset	Scale	Metrics	GF [21]	SD [19]	GSRPT [42]	MSG [26]	DKN [28]	FDKN [28]	PMBANet [68]	FDSR [23]	JIIF [59]	DCTNet [74]	LGR [11]	DADA [44]	DSR-EI	DSR-EI ⁺
Middlebury	4×	MSE	33.3	24.9	39.8	4.13	4.29	3.60	4.72	7.72	2.70	5.00	3.04	2.58	2.46	2.56
		MAE	1.27	0.46	0.79	0.22	0.18	0.16	0.25	0.35	0.11	0.24	0.13	0.11	0.08	0.07
	8×	MSE	40.5	82.5	32.7	10.5	11.2	10.4	9.48	23.2	8.01	15.1	7.26	5.68	6.20	5.13
		MAE	1.49	0.86	0.82	0.43	0.38	0.37	0.38	0.69	0.27	0.57	0.24	0.20	0.18	0.18
NYUv2	16×	MSE	67.4	511	41.5	34.2	47.6	38.5	30.6	55.4	37.5	52.3	24.7	16.3	15.8	16.6
		MAE	2.21	1.73	1.24	1.06	1.42	1.18	0.89	1.51	0.98	1.50	0.67	0.48	0.47	0.40
	4×	MSE	114	36.0	112	6.85	11.4	9.07	10.8	10.1	3.28	3.63	6.45	4.83	2.82	2.75
		MAE	3.91	1.31	3.61	0.81	1.03	0.85	0.93	0.94	0.52	0.68	0.73	0.64	0.49	0.47
DIML	8×	MSE	142	105	122	24.1	29.8	29.9	17.2	19.5	15.2	20.9	19.6	16.6	11.8	11.8
		MAE	4.47	2.57	3.86	1.66	1.82	1.80	1.38	1.38	1.29	1.79	1.42	1.30	1.12	1.09
	16×	MSE	249	533	219	84.5	115	113	84.9	86.4	59.9	77.0	67.5	59.0	47.8	47.1
		MAE	6.34	5.07	5.40	3.35	4.01	3.95	3.26	3.35	2.81	3.61	2.90	2.64	2.48	2.40
DIML	4×	MSE	25.6	10.5	20.7	1.73	3.47	2.20	3.05	2.75	1.19	2.09	1.68	1.33	0.70	0.65
		MAE	1.45	0.40	1.15	0.22	0.33	0.23	0.31	0.29	0.16	0.31	0.20	0.17	0.13	0.12
	8×	MSE	34.1	44.9	23.0	4.13	5.47	5.95	5.87	8.40	3.65	7.08	3.51	2.93	2.12	2.09
		MAE	1.77	0.83	1.26	0.40	0.45	0.47	0.47	0.66	0.32	0.65	0.31	0.28	0.22	0.22
DIML	16×	MSE	66.3	41.1	39.3	13.0	19.3	20.8	13.8	32.9	11.7	23.4	9.45	7.61	6.29	6.31
		MAE	2.74	1.91	1.78	0.93	1.20	1.24	0.87	1.66	0.81	1.75	0.68	0.59	0.52	0.50

Table 1: **Results on Middlebury, NYUv2 and DIML datasets.** The lower the MSE and MAE, the better.

Scale	SDF [36]	SVLRM [45]	DJF [36]	DJFR [37]	PAC [58]	CUNet [12]	FDKN [28]	DKN [28]	FDSR [23]	DCTNet [74]	RSAG [69]	DSR-EI	DSR-EI ⁺
4×	2.00	3.39	3.41	3.35	1.25	1.18	1.18	1.30	1.16	1.07	1.14	0.91	0.91
8×	3.23	5.59	5.57	5.57	1.98	1.95	1.91	1.96	1.82	1.78	1.75	1.37	1.38
16×	5.16	8.28	8.15	7.99	3.49	3.45	3.41	3.42	3.06	3.18	2.96	2.10	2.10

Table 2: **Results on the RGBDD dataset.** We report RMSE, the lower the better.

respectively. When evaluating results on a specific dataset, we do not perform any pre-training on the others. Following [11], testing is performed by processing 256×256 patches at a time on Middlebury, NYUv2 and DIML for fairness, while full-resolution images are processed for RGBDD.

4.3. Comparison with State-of-the-Art

We compare DSR-EI to GF [21], SD [19], GSRPT [42], MSG [26], DKN and its fast implementation FDKN [28], PMBANet [68], FDSR [23], JIIF [59], DCTNet [74], LGR [11], and finally to DADA [44] on Middlebury, NYUv2 and DIML datasets. We could not compare with PDR-Net [40] under the same setting because the source code is unavailable at the time of writing. For the other methods, we use the results from [11] or the officially published codes, and results from [69, 44] for concurrent works. On the RGBDD dataset, the proposed network is compared to SDF [36], SVLRM [45], DJF [36], DJFR [37], PAC [58], CUNet [12], FDKN [28], DKN [28], FDSR [23], DCTNet [74] and RASG [69]. To be fair with DCTNet [74], we downsample depth maps as the LR input. When reporting results, we highlight **absolute**, **second** and **third** best methods for each metric on each dataset.

Quantitative Comparison. Tabs. 1 and 2 report the accuracy of super-solved depth maps at factors 4×, 8× and 16× on the four datasets. As expected, learning-based methods show a significant improvement over traditional methods [21, 19, 42]. DSR-EI vastly outperforms any ex-

isting network, with larger gaps in accuracy with the increasing of the upsampling factor. This can be attributed to the limitations affecting existing methods, i.e., 1) the guidance of either explicit or implicit RGB features alone being insufficient; 2) multi-modal information fusion on a single scale being not flexible enough to deal with complex scenes. Both limitations are fully addressed by DSR-EI, which consistently outperforms concurrent works [44, 69].

The margin is consistent both on perfect (Middlebury) and noisy datasets (NYUv2, DIML, RGBDD), with the latter being a more challenging, realistic benchmark. Although DSR-EI⁺ is definitely the absolute best, its margin over DSR-EI is negligible, with tiny gains yielded by NL-SPN with respect to our main modules. Indeed, DSR-EI alone consistently outperforms any other approach already.

Qualitative Comparison. Fig. 7 shows qualitative comparisons of 8× super-solved depth maps on Middlebury, NYUv2 and DIML datasets, respectively. From left to right, we show, the RGB image and LR depth map, followed by the ground truth HR depth and error maps obtained by several state-of-the-art frameworks, concluding with ours in the second-to-last columns. In each of the three examples, the lower error magnitude produced by DSR-EI⁺ further demonstrates its superior accuracy.

Cross-dataset Generalization. We conclude the comparison with existing methods by conducting cross-dataset experiments with 8× factor. All methods are trained on the NYUv2 dataset and directly evaluated on DIML and Middlebury. Table 3 collects quantitative results for the 11

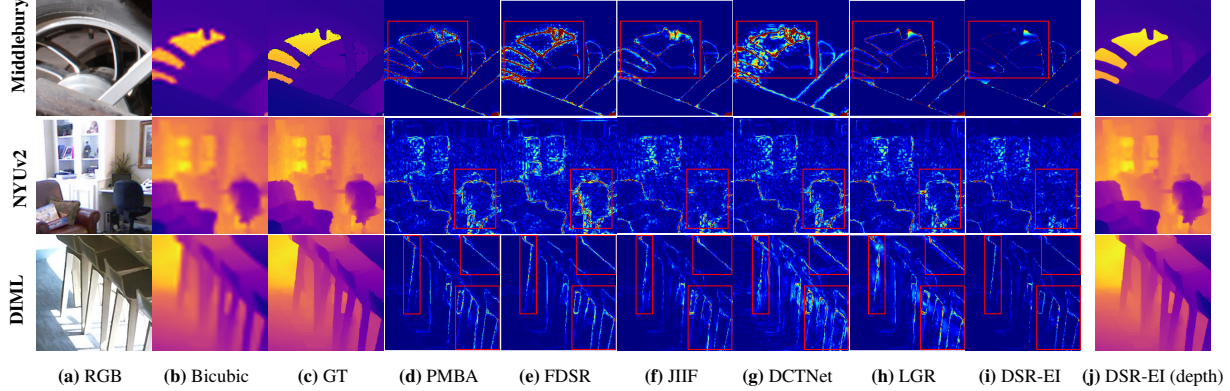


Figure 7: **Qualitative comparison on Middlebury, NYUv2 and DIML datasets (scaling factor 8 \times).** From left to right: (a) RGB image, (b) Bicubic upsampled depth map, (c) GT; then, error maps achieved by selected methods: (d) PMBA [68], (e) FDSR [23], (f) JIIF [59], (g) DCTNet [74], (h) LGR [11]; finally, (i) error maps and (j) predictions by DSR-EI.

Testing Dataset	Metric	GF[21]	SD [19]	GSRPT [42]	MSG [26]	FDKN [28]	PMBANet [68]	FDSR [23]	JIIF [59]	DCTNet [74]	LGR [11]	DSR-EI ⁺
DIML	MSE	34.1	44.9	23.0	5.76	6.74	7.35	7.73	4.10	5.64	4.95	3.72
	MAE	1.77	0.83	1.26	0.51	0.53	0.59	0.74	0.38	0.77	0.40	0.36
Middlebury- <i>HR</i>	MSE	40.5	82.5	32.7	11.0	10.0	9.62	18.4	19.3	17.5	8.25	14.6
	MAE	1.49	0.86	0.82	0.54	0.43	0.46	0.73	0.74	0.77	0.35	0.54
Middlebury- <i>LR</i>	MSE	25.6	28.8	15.8	8.89	5.54	4.16	6.92	4.40	6.96	5.94	3.44
	MAE	2.31	2.07	1.73	1.62	0.99	0.91	1.09	0.92	1.15	1.11	0.87

Table 3: **Cross-dataset generalization.** All methods are trained on NYUv2 and tested on DIML/Middlebury with factor 8 \times . Middlebury-*HR* is the test set defined in [11], Middlebury-*LR* is the one from [59]. The lower MSE and MAE, the better.

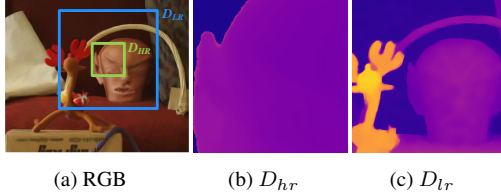


Figure 8: **Image context processed on Middlebury - HR vs LR.** (a) RGB image and depth patches D processed when testing on (b) Middlebury-*HR* and (c) Middlebury-*LR*.

selected methods. Again, CNN-based methods attain better performance than traditional approaches, despite the domain gap playing a significant role in performance – as evident by comparing results with Table 3. Nonetheless, DSR-EI outperforms any other framework on DIML.

When considering the Middlebury dataset, we evaluate using the setting proposed in [11] – Middlebury-*HR* in the table. In this case, our results are slightly less accurate compared to a few existing methods. However, given the very high resolution of Middlebury images, we argue that this testing protocol – i.e., consisting of processing 256 \times 256 crops at a time – penalizes our network’s ability to leverage the global context in the input that results irremediably reduced to a very local area in these images. Therefore, we also evaluate on Middlebury test set defined by [59]

– Middlebury-*LR* in the table. Note that different subsets of images are used in Middlebury-*HR* and Middlebury-*LR* splits. Besides, Middlebury-*LR* images are resized and processed without cropping, i.e., used at full-size after resizing, allowing to fully exploit global context, while this is not feasible with Middlebury-*HR* due to memory constraints. In this case, DSR-EI attains the best performance again, confirming our previous analysis, as shown in Tab. 3. Such a difference in terms of context is highlighted in Fig. 8.

4.4. Ablation Study

We now perform a series of ablation experiments to measure the impact of key components and parameters in DSR-EI. Tab. 4 collects the outcome of these studies, conducted on NYUv2 test set with 8 \times factor. Without loss of fairness, NLSPN is never used here – to fully focus on the impact of single components.

(a) Implicit vs Explicit High-Frequency Features. To measure the impact of both implicit and explicit HR features, we compare the performance of the proposed network and its variants when extracting either only one of the two. The quantitative results are collected in Tab. 4(a). Without the help of gradient maps (I), the performance of the network significantly degrades. We believe this is caused by the difficulty in effectively extracting fine structures or salient edges required for LR depth maps from implicit HF

No. Gradient	Shallow Feature	LCF	ResBlock	MSE	MAE	No. HF Information	MSE	MAE
(I)	X	✓	✓	13.1	1.19	(I) Canny Edge	12.0	1.13
(II)	✓	X		12.4	1.14	(II) Gaussian Edge	12.1	1.16
(III)	✓	✓	✓	12.3	1.15	(IV) DCT	12.1	1.15
(IV)	✓	✓	✓	11.8	1.12	(V) Wavelet Transform	12.1	1.15
						(V) Gradient Map	11.8	1.12

No. Config.	Params (M)	Flops (G)	MSE	MAE	No. Scales	Params (M)	MSE	MAE
(I) EdgeNet [41]	5.78	95.6	12.0	1.12	(I) H1	1.5	12.3	1.14
(II) SCPA [73]	0.29	13.1	12.5	1.16	(II) H1, H2	3.0	11.8	1.12
(III) HFEB	0.27	11.6	11.8	1.12	(III) H1, H2, H3	4.5	11.8	1.12

No. Config.	Params (M)	MSE	MAE	No. Stages	Params (M)	MSE	MAE
(I) w/o AFFM	-	12.7	1.16	(I) 1	14.2	13.3	1.19
(II) w/o att	1.3	12.2	1.13	(II) 2	25.0	11.8	1.12
(III) Concat.	4.5	12.2	1.13	(III) 3	37.5	11.6	1.10
(IV) AFFM	3.0	11.8	1.12				

Table 4: **Ablation study (NYUv2 test set, 8× factor).** We measure the impact of (a) explicit vs implicit HR features, (b) different kinds of HF supervision, (c) different sub-networks for explicit HF features extraction, (d) scales at which AFFM is applied, (e) modules building AFFM, (f) number of stages in GDRB. In yellow, configurations corresponding to our final model without NLSPN.

features alone. Moreover, explicit features highlight regions in the image that need to be focused on, avoiding DSR-EI to learn to localize them and easing its task.

Nonetheless, explicit HF features alone as guidance (II) are insufficient as well. We argue that the explicit information might neglect some RGB features, whereas implicit HF feature extraction can recover them. Furthermore, to verify the effectiveness of LCF, we replace it with ResBlock [22] (III) to extract shallow features from RGB images, highlighting a negative impact on implicit features extraction – i.e., it results less accurate than (II).

(b) Ablation on Explicit High-Frequency Features.

We now investigate which kind of HF information is more effective for our framework. Purposefully, we train HFEB with supervision coming from five different HF features used as ground truth edge maps E_{gt} . Tab. 4(b) collects results from this experiment, highlighting that Canny edges (I) and Gradient maps (V) lead to slightly better results.

(c) Impact of HFEB. To verify the effectiveness of HFEB, we replace it with EdgeNet [41] – based on the widely-used U-net structure – and SCPA [73], which inspires our scaling strategy. As shown in Tab. 4(c), EdgeNet (I) achieves lower MSE and MAE than SCPA (II), yet needs more parameters – 5.78M vs. 0.29M. HFEB (III) yields the same accuracy as EdgeNet, with fewer parameters than SCPA, thus being both more accurate and efficient.

(d – e) Impact of AFFM. We now measure the effectiveness of AFFM. Tab. 4(d) shows results obtained by deploying AFFM at different scales, respectively the highest (I), the first two (II) and all of the three scales. We can notice how performing fusion at the highest scale alone results insufficient, whereas using multi-scale features for fusion

	PMBANet [68]	FDSR [23]	JIIF [59]	DCTNet [74]	LGR [11]	Ours
Runtime (ms)	26.9	1.03	89.8	9.03	26.4	51.5
Memory Peak (GB)	3.07	2.05	2.36	0.26	0.19	18.6

Table 5: **Computational requirements.** Experiments on Nvidia RTX 3090 GPU, with 256×256 input and 8× factor.

yields improvements, despite saturating already when using two scales, with the lowest one not providing additional, meaningful details to be taken into account.

Furthermore, we ablate AFFM in its single components. Tab. 4(e) resumes the outcome of this evaluation. We first test the performance of DSR-EI without AFFM (I), highlighting a large drop in accuracy. By adding dynamic fusion, yet without using attention (II) vastly improves the results already, while replacing the weighted sum in the upper of Fig. 5 with concatenation and a ResBlock [22] (III) yields worse results compared to our full AFFM (IV).

(f) Impact of Stages Number. To conclude, we evaluate the impact of the multi-stage design. As shown in Tab. 4(f), a single-stage architecture (I) is vastly outperformed by deploying two stages (II), yet at the expense of doubling the number of parameters. Furthermore, while the three-stage architecture (III) still yields some improvement, the benefit is minor in comparison to the significant increase in parameters. Hence, we choose two stages as the default configuration to balance accuracy and efficiency.

4.5. Limitations

We conclude by listing a few limitations of DSR-EI. As previously pointed out, global context is crucial for it to achieve the best performance. When this is unavailable, some accuracy is lost when generalizing across datasets. Moreover, the significant improvements over existing methods are paid for in terms of time/memory requirements. Tab. 5 highlights the higher runtime and, more evidently, peak memory usage. Future work will aim at reducing the overhead, while minimizing the drop in accuracy.

5. Conclusion

This paper proposed DSR-EI, a depth super-resolution network, which includes a high-frequency extraction branch (HFEB) and a guided depth restoration branch (GDRB). Specifically, implemented as an efficient transformer, HFEB extracts explicit HF features. Then, GDRB deploys a two-stage encoder-decoder network to recover HR depth maps progressively, by adaptively fusing discriminative features while supplementing additional, implicit HF information. Exhaustive experiments demonstrate that DSR-EI sets a new state-of-the-art for guided depth super-resolution.

Acknowledgments

We acknowledge supports by the National Natural Science Foundation of China (No.61627811), Natural Science Foundation of Shaanxi Province (No. 2021JZ-04), Joint project of key R&D universities in Shaanxi Province (No. 2021GXZH-Z-093), and the China Scholarship Council (CSC).

References

- [1] Cyrus Bamji, John Godbaz, Minseok Oh, Swati Mehta, Andrew Payne, Sergio Ortiz, Satyadev Nagaraja, Travis Perry, and Barry Thompson. A review of indirect time-of-flight technologies. *IEEE Transactions on Electron Devices*, 2022. 1
- [2] Qin Cai, David Gallup, Cha Zhang, and Zhengyou Zhang. 3d deformable face tracking with a commodity depth camera. In *European conference on computer vision*, pages 229–242. Springer, 2010. 1
- [3] Nicolas Carion, Francisco Massa, Gabriel Synnaeve, Nicolas Usunier, Alexander Kirillov, and Sergey Zagoruyko. End-to-end object detection with transformers. In *European conference on computer vision*, pages 213–229. Springer, 2020. 2
- [4] Chin-Chen Chang, Chia-Chen Lin, Chun-Sen Tseng, and Wei-Liang Tai. Reversible hiding in dct-based compressed images. *Information Sciences*, 177(13):2768–2786, 2007. 5
- [5] Xiaokang Chen, Kwan-Yee Lin, Chen Qian, Gang Zeng, and Hongsheng Li. 3d sketch-aware semantic scene completion via semi-supervised structure prior. In *Proceedings of the IEEE/CVF Conference on Computer Vision and Pattern Recognition*, pages 4193–4202, 2020. 1
- [6] Xiaokang Chen, Yajie Xing, and Gang Zeng. Real-time semantic scene completion via feature aggregation and conditioned prediction. In *2020 IEEE International Conference on Image Processing (ICIP)*, pages 2830–2834. IEEE, 2020. 1
- [7] Yinpeng Chen, Xiyang Dai, Mengchen Liu, Dongdong Chen, Lu Yuan, and Zicheng Liu. Dynamic convolution: Attention over convolution kernels. In *Proceedings of the IEEE/CVF Conference on Computer Vision and Pattern Recognition*, pages 11030–11039, 2020. 4
- [8] Yilun Chen, Zhicheng Wang, Yuxiang Peng, Zhiqiang Zhang, Gang Yu, and Jian Sun. Cascaded pyramid network for multi-person pose estimation. In *Proceedings of the IEEE conference on computer vision and pattern recognition*, pages 7103–7112, 2018. 1
- [9] Zuyao Chen, Runmin Cong, Qianqian Xu, and Qingming Huang. Dpanet: Depth potentiality-aware gated attention network for rgb-d salient object detection. *IEEE Transactions on Image Processing*, 30:7012–7024, 2021. 1
- [10] Jaehoon Cho, Dongbo Min, Youngjung Kim, and Kwanghoon Sohn. Deep monocular depth estimation leveraging a large-scale outdoor stereo dataset. *Expert Systems with Applications*, 178:114877, 2021. 5
- [11] Riccardo de Lutio, Alexander Becker, Stefano D’Aronco, Stefania Russo, Jan D Wegner, and Konrad Schindler. Learn-
- [12] Xin Deng and Pier Luigi Dragotti. Deep convolutional neural network for multi-modal image restoration and fusion. *IEEE transactions on pattern analysis and machine intelligence*, 43(10):3333–3348, 2020. 6
- [13] James Diebel and Sebastian Thrun. An application of markov random fields to range sensing. *Advances in neural information processing systems*, 18, 2005. 1, 2
- [14] Alexey Dosovitskiy, Lucas Beyer, Alexander Kolesnikov, Dirk Weissenborn, Xiaohua Zhai, Thomas Unterthiner, Mostafa Dehghani, Matthias Minderer, Georg Heigold, and Sylvain and Gelly. An image is worth 16x16 words: Transformers for image recognition at scale. In *International Conference on Learning Representations*, 2021. 2
- [15] Yazan Abu Farha and Jurgen Gall. Ms-tcn: Multi-stage temporal convolutional network for action segmentation. In *Proceedings of the IEEE/CVF Conference on Computer Vision and Pattern Recognition*, pages 3575–3584, 2019. 1
- [16] David Ferstl, Christian Reinbacher, Rene Ranftl, Matthias Rüther, and Horst Bischof. Image guided depth upsampling using anisotropic total generalized variation. In *Proceedings of the IEEE international conference on computer vision*, pages 993–1000, 2013. 1, 2
- [17] Hongyun Gao, Xin Tao, Xiaoyong Shen, and Jiaya Jia. Dynamic scene deblurring with parameter selective sharing and nested skip connections. In *Proceedings of the IEEE/CVF conference on computer vision and pattern recognition*, pages 3848–3856, 2019. 4
- [18] Liuhan Ge, Hui Liang, Junsong Yuan, and Daniel Thalmann. Real-time 3d hand pose estimation with 3d convolutional neural networks. *IEEE Transactions on Pattern Analysis and Machine Intelligence*, 41(4):956–970, 2019. 1
- [19] Bumsub Ham, Minsu Cho, and Jean Ponce. Robust guided image filtering using nonconvex potentials. *IEEE transactions on pattern analysis and machine intelligence*, 40(1):192–207, 2017. 6, 7
- [20] Kai Han, Yunhe Wang, Hanting Chen, Xinghao Chen, Jianyu Guo, Zhenhua Liu, Yehui Tang, An Xiao, Chunjing Xu, Yixing Xu, et al. A survey on vision transformer. *IEEE transactions on pattern analysis and machine intelligence*, 2022. 2
- [21] Kaiming He, Jian Sun, and Xiaou Tang. Guided image filtering. In *European conference on computer vision*, pages 1–14. Springer, 2010. 6, 7
- [22] Kaiming He, Xiangyu Zhang, Shaoqing Ren, and Jian Sun. Deep residual learning for image recognition. In *Proceedings of the IEEE conference on computer vision and pattern recognition*, pages 770–778, 2016. 4, 8
- [23] Lingzhi He, Hongguang Zhu, Feng Li, Huihui Bai, Runmin Cong, Chunjie Zhang, Chunyu Lin, Meiqin Liu, and Yao Zhao. Towards fast and accurate real-world depth super-resolution: Benchmark dataset and baseline. In *Proceedings of the IEEE/CVF Conference on Computer Vision and Pattern Recognition*, pages 9229–9238, 2021. 5, 6, 7, 8

[24] Heiko Hirschmuller and Daniel Scharstein. Evaluation of cost functions for stereo matching. In *2007 IEEE Conference on Computer Vision and Pattern Recognition*, pages 1–8. IEEE, 2007. 5

[25] Tao Huang, Lang Huang, Shan You, Fei Wang, Chen Qian, and Chang Xu. Lightvit: Towards light-weight convolution-free vision transformers. *arXiv preprint arXiv:2207.05557*, 2022. 3, 4

[26] Tak-Wai Hui, Chen Change Loy, and Xiaoou Tang. Depth map super-resolution by deep multi-scale guidance. In *European conference on computer vision*, pages 353–369. Springer, 2016. 1, 2, 6, 7

[27] Martin Kiechle, Simon Hawe, and Martin Kleinsteuber. A joint intensity and depth co-sparse analysis model for depth map super-resolution. In *Proceedings of the IEEE international conference on computer vision*, pages 1545–1552, 2013. 2

[28] Beomjun Kim, Jean Ponce, and Bumsub Ham. Deformable kernel networks for joint image filtering. *International Journal of Computer Vision*, 129(2):579–600, 2021. 2, 6, 7

[29] Kiyeon Kim, Seungyong Lee, and Sunghyun Cho. Mssnet: Multi-scale-stage network for single image deblurring. *arXiv preprint arXiv:2202.09652*, 2022. 2

[30] Sunok Kim, Dongbo Min, Bumsub Ham, Seungryong Kim, and Kwanghoon Sohn. Deep stereo confidence prediction for depth estimation. In *2017 ieee international conference on image processing (icip)*, pages 992–996. IEEE, 2017. 5

[31] Youngjung Kim, Bumsub Ham, Changjae Oh, and Kwanghoon Sohn. Structure selective depth superresolution for rgb-d cameras. *IEEE Transactions on Image Processing*, 25(11):5227–5238, 2016. 5

[32] Youngjung Kim, Hyungjoo Jung, Dongbo Min, and Kwanghoon Sohn. Deep monocular depth estimation via integration of global and local predictions. *IEEE transactions on Image Processing*, 27(8):4131–4144, 2018. 5

[33] Johannes Kopf, Michael F Cohen, Dani Lischinski, and Matt Uyttendaele. Joint bilateral upsampling. *ACM Transactions on Graphics (ToG)*, 26(3):96–es, 2007. 1, 2

[34] HyeokHyen Kwon, Yu-Wing Tai, and Stephen Lin. Data-driven depth map refinement via multi-scale sparse representation. In *Proceedings of the IEEE conference on computer vision and pattern recognition*, pages 159–167, 2015. 2

[35] Youngwan Lee, Jonghee Kim, Jeffrey Willette, and Sung Ju Hwang. Mpvit: Multi-path vision transformer for dense prediction. In *Proceedings of the IEEE/CVF Conference on Computer Vision and Pattern Recognition*, pages 7287–7296, 2022. 2

[36] Yijun Li, Jia-Bin Huang, Narendra Ahuja, and Ming-Hsuan Yang. Deep joint image filtering. In *European conference on computer vision*, pages 154–169. Springer, 2016. 1, 2, 6

[37] Yijun Li, Jia-Bin Huang, Narendra Ahuja, and Ming-Hsuan Yang. Joint image filtering with deep convolutional networks. *IEEE transactions on pattern analysis and machine intelligence*, 41(8):1909–1923, 2019. 1, 2, 6

[38] Yu Li, Dongbo Min, Minh N Do, and Jiangbo Lu. Fast guided global interpolation for depth and motion. In *European Conference on Computer Vision*, pages 717–733. Springer, 2016. 1, 2

[39] Shinfeng D Lin, Shih-Chieh Shie, and Jim Yi Guo. Improving the robustness of dct-based image watermarking against jpeg compression. *Computer Standards & Interfaces*, 32(1-2):54–60, 2010. 5

[40] Peng Liu, Zonghua Zhang, Zhaozong Meng, Nan Gao, and Chao Wang. Pdr-net: Progressive depth reconstruction network for color guided depth map super-resolution. *Neurocomputing*, 479:75–88, 2022. 5, 6

[41] Yang Liu, Farming Fang, Tingting Wang, Juncheng Li, Yun Sheng, and Guixu Zhang. Multi-scale grid network for image deblurring with high-frequency guidance. *IEEE Transactions on Multimedia*, 2021. 2, 4, 5, 8

[42] Riccardo de Lutio, Stefano D’aronco, Jan Dirk Wegner, and Konrad Schindler. Guided super-resolution as pixel-to-pixel transformation. In *Proceedings of the IEEE/CVF International Conference on Computer Vision*, pages 8829–8837, 2019. 1, 2, 6, 7

[43] Oisin Mac Aodha, Neill DF Campbell, Arun Nair, and Gabriel J Brostow. Patch based synthesis for single depth image super-resolution. In *European conference on computer vision*, pages 71–84. Springer, 2012. 2

[44] Nando Metzger, Rodrigo Caye Daudt, and Konrad Schindler. Guided depth super-resolution by deep anisotropic diffusion. *arXiv preprint arXiv:2211.11592*, 2022. 2, 6

[45] Jinshan Pan, Jiangxin Dong, Jimmy S Ren, Liang Lin, Jin-hui Tang, and Ming-Hsuan Yang. Spatially variant linear representation models for joint filtering. In *Proceedings of the IEEE/CVF Conference on Computer Vision and Pattern Recognition*, pages 1702–1711, 2019. 6

[46] Jinsun Park, Kyungdon Joo, Zhe Hu, Chi-Kuei Liu, and In So Kweon. Non-local spatial propagation network for depth completion. In *European Conference on Computer Vision*, pages 120–136. Springer, 2020. 5

[47] Jaesik Park, Hyeongwoo Kim, Yu-Wing Tai, Michael S Brown, and Inso Kweon. High quality depth map upsampling for 3d-tof cameras. In *2011 International Conference on Computer Vision*, pages 1623–1630. IEEE, 2011. 1, 2

[48] Adam Paszke, Sam Gross, Francisco Massa, Adam Lerer, James Bradbury, Gregory Chanan, Trevor Killeen, Zeming Lin, Natalia Gimelshein, Luca Antiga, et al. Pytorch: An imperative style, high-performance deep learning library. *Advances in neural information processing systems*, 32, 2019. 5

[49] Mengyang Pu, Yaping Huang, Yuming Liu, Qingji Guan, and Haibin Ling. Edter: Edge detection with transformer. In *Proceedings of the IEEE/CVF Conference on Computer Vision and Pattern Recognition*, pages 1402–1412, 2022. 2, 3

[50] Zequn Qin, Pengyi Zhang, Fei Wu, and Xi Li. Fcanet: Frequency channel attention networks. In *Proceedings of the IEEE/CVF international conference on computer vision*, pages 783–792, 2021. 5

[51] AK Riemens, OP Gangwal, B Barenbrug, and R-PM Berretty. Multistep joint bilateral depth upsampling. In *Visual communications and image processing 2009*, volume 7257, pages 192–203. SPIE, 2009. 1, 2

[52] Olaf Ronneberger, Philipp Fischer, and Thomas Brox. U-net: Convolutional networks for biomedical image segmentation. In *International Conference on Medical image computing and computer-assisted intervention*, pages 234–241. Springer, 2015. 4

[53] Paul-Edouard Sarlin, Cesar Cadena, Roland Siegwart, and Marcin Dymczyk. From coarse to fine: Robust hierarchical localization at large scale. In *Proceedings of the IEEE/CVF Conference on Computer Vision and Pattern Recognition*, pages 12716–12725, 2019. 4

[54] Daniel Scharstein, Heiko Hirschmüller, York Kitajima, Greg Krathwohl, Nera Nešić, Xi Wang, and Porter Westling. High-resolution stereo datasets with subpixel-accurate ground truth. In *German conference on pattern recognition*, pages 31–42. Springer, 2014. 5

[55] Daniel Scharstein and Chris Pal. Learning conditional random fields for stereo. In *2007 IEEE Conference on Computer Vision and Pattern Recognition*, pages 1–8. IEEE, 2007. 5

[56] Daniel Scharstein and Richard Szeliski. High-accuracy stereo depth maps using structured light. In *2003 IEEE Computer Society Conference on Computer Vision and Pattern Recognition, 2003. Proceedings.*, volume 1, pages I–I. IEEE, 2003. 5

[57] Nathan Silberman, Derek Hoiem, Pushmeet Kohli, and Rob Fergus. Indoor segmentation and support inference from rgbd images. In *European conference on computer vision*, pages 746–760. Springer, 2012. 5

[58] Hang Su, Varun Jampani, Deqing Sun, Orazio Gallo, Erik Learned-Miller, and Jan Kautz. Pixel-adaptive convolutional neural networks. In *Proceedings of the IEEE/CVF Conference on Computer Vision and Pattern Recognition*, pages 11166–11175, 2019. 6

[59] Jiaxiang Tang, Xiaokang Chen, and Gang Zeng. Joint implicit image function for guided depth super-resolution. In *Proceedings of the 29th ACM International Conference on Multimedia*, pages 4390–4399, 2021. 1, 2, 4, 6, 7, 8

[60] Qi Tang, Runmin Cong, Ronghui Sheng, Lingzhi He, Dan Zhang, Yao Zhao, and Sam Kwong. Bridgenet: A joint learning network of depth map super-resolution and monocular depth estimation. In *Proceedings of the 29th ACM International Conference on Multimedia*, pages 2148–2157, 2021. 1

[61] Hugo Touvron, Matthieu Cord, Matthijs Douze, Francisco Massa, Alexandre Sablayrolles, and Hervé Jégou. Training data-efficient image transformers & distillation through attention. In *International Conference on Machine Learning*, pages 10347–10357. PMLR, 2021. 2

[62] Ashish Vaswani, Noam Shazeer, Niki Parmar, Jakob Uszkoreit, Llion Jones, Aidan N Gomez, Łukasz Kaiser, and Illia Polosukhin. Attention is all you need. *Advances in neural information processing systems*, 30, 2017. 2, 3

[63] Huiyu Wang, Aniruddha Kembhavi, Ali Farhadi, Alan L Yuille, and Mohammad Rastegari. Elastic: Improving cnns with dynamic scaling policies. In *Proceedings of the IEEE/CVF Conference on Computer Vision and Pattern Recognition*, pages 2258–2267, 2019. 3

[64] Wenhui Wang, Enze Xie, Xiang Li, Deng-Ping Fan, Kaitao Song, Ding Liang, Tong Lu, Ping Luo, and Ling Shao. Pyramid vision transformer: A versatile backbone for dense prediction without convolutions. In *Proceedings of the IEEE/CVF International Conference on Computer Vision*, pages 568–578, 2021. 2

[65] Yongzhe Wang, Antonio Ortega, Dong Tian, and Anthony Vetro. A graph-based joint bilateral approach for depth enhancement. In *2014 IEEE International Conference on Acoustics, Speech and Signal Processing (ICASSP)*, pages 885–889. IEEE, 2014. 1, 2

[66] Zhihui Wang, Xinchen Ye, Baoli Sun, Jingyu Yang, Rui Xu, and Haojie Li. Depth upsampling based on deep edge-aware learning. *Pattern Recognition*, 103:107274, 2020. 1, 2, 3

[67] Qingxiong Yang, Ruigang Yang, James Davis, and David Nistér. Spatial-depth super resolution for range images. In *2007 IEEE Conference on Computer Vision and Pattern Recognition*, pages 1–8. IEEE, 2007. 1, 2

[68] Xinchen Ye, Baoli Sun, Zhihui Wang, Jingyu Yang, Rui Xu, Haojie Li, and Baopu Li. Pmbanet: Progressive multi-branch aggregation network for scene depth super-resolution. *IEEE Transactions on Image Processing*, 29:7427–7442, 2020. 1, 2, 4, 5, 6, 7, 8

[69] Jiayi Yuan, Haobo Jiang, Xiang Li, Jianjun Qian, Jun Li, and Jian Yang. Recurrent structure attention guidance for depth super-resolution. *arXiv preprint arXiv:2301.13419*, 2023. 2, 6

[70] Syed Waqas Zamir, Aditya Arora, Salman Khan, Munawar Hayat, Fahad Shahbaz Khan, and Ming-Hsuan Yang. Restormer: Efficient transformer for high-resolution image restoration. In *Proceedings of the IEEE/CVF Conference on Computer Vision and Pattern Recognition*, pages 5728–5739, 2022. 2

[71] Syed Waqas Zamir, Aditya Arora, Salman Khan, Munawar Hayat, Fahad Shahbaz Khan, Ming-Hsuan Yang, and Ling Shao. Multi-stage progressive image restoration. In *Proceedings of the IEEE/CVF conference on computer vision and pattern recognition*, pages 14821–14831, 2021. 2, 4

[72] Yulun Zhang, Kunpeng Li, Kai Li, Lichen Wang, Bineng Zhong, and Yun Fu. Image super-resolution using very deep residual channel attention networks. In *Proceedings of the European conference on computer vision (ECCV)*, pages 286–301, 2018. 3, 4

[73] Hengyuan Zhao, Xiangtao Kong, Jingwen He, Yu Qiao, and Chao Dong. Efficient image super-resolution using pixel attention. In *European Conference on Computer Vision Workshops*, pages 56–72. Springer, 2020. 3, 4, 8

[74] Zixiang Zhao, Jiangshe Zhang, Shuang Xu, Zudi Lin, and Hanspeter Pfister. Discrete cosine transform network for guided depth map super-resolution. In *Proceedings of the IEEE/CVF Conference on Computer Vision and Pattern Recognition*, pages 5697–5707, 2022. 2, 6, 7, 8

[75] Xueyan Zou, Fanyi Xiao, Zhiding Yu, Yuheng Li, and Yong Jae Lee. Delving deeper into anti-aliasing in convnets. *International Journal of Computer Vision*, pages 1–15, 2022. 4

[76] Yifan Zuo, Yuming Fang, Ping An, Xiwu Shang, and Junnan Yang. Frequency-dependent depth map enhancement via iterative depth-guided affine transformation and intensity-

guided refinement. *IEEE Transactions on Multimedia*, 23:772–783, 2020. [1](#), [2](#)